TRENDS IN SCIENCES 2026; 23(2): 11560
https://doi.org/10.48048/tis.2026.11560
RESEARCH ARTICLE

Mineralogical and Geochemical Analysis of Mining and Petroleum Rocks in the Khorat Plateau: Implications for CO_2 Mineralization and CCS

Vimoltip Singtuen[1,*], Juthatip Khonman[1,2] and Puracheth Rithchumpon[3]

[1]*Department of Geotechnology, Faculty of Technology, Khon Kaen University, Khon Kaen 40002 Thailand*
[2]*PTT Exploration and Production, Enco Building A, Vibhavadi Rangist Road, Chatuchak, Bangkok, Thailand*
[3]*Department of Chemistry, Faculty of Science, Khon Kaen University, Khon Kaen 40002 Thailand*

([*]Corresponding author's e-mail: vimoltipst@gmail.com)

Received: 10 August 2025, Revised: 22 August 2025, Accepted: 10 September 2025, Published: 1 December 2025

Abstract

Rising CO_2 emissions from energy and industrial sectors underscore the urgent need for effective carbon capture and storage (CCS) strategies, with geological sequestration offering long-term mitigation potential. The Khorat Plateau in northeastern Thailand hosts diverse lithologies - Permian carbonates, Khorat Group sandstones, evaporitic rock salt, and Cenozoic basalts - associated with active mining and petroleum activities. While previous studies have examined CO_2 - rock interactions in specific formations such as mudstones of the Triassic Huai Hin Lat Formation, limited data exist on the comparative reactivity of multiple lithologies under wet CO_2 conditions. This study evaluates the mineralogical and geochemical responses of representative rock types, including sandstone, calcareous sandstone, limestone, basalt, and rock salt, collected from boreholes and mining sites across the Khorat Plateau. Controlled laboratory experiments involved CO_2 exposure in the presence of water, with pre- and post-reaction analyses conducted using X-ray diffraction (XRD) and X-ray fluorescence (XRF). Results show that limestone and basalt exhibit the highest reactivity, forming stable secondary phases such as wollastonite ($CaSiO_3$), portlandite ($Ca(OH)_2$), amorphous CaO, and phyllosilicates, indicating significant potential for mineral trapping. Basalt, in particular, underwent pronounced alteration of primary silicate minerals, while sandstone, calcareous sandstone, and rock salt showed minimal mineralogical changes. These lithology-dependent reactivity patterns highlight basalt and limestone as promising candidates for CCS deployment in the Khorat Plateau, despite earlier reservations regarding basalt suitability. The findings provide the 1st integrated comparison of multiple lithologies from both mining and petroleum contexts in the region, bridging a critical knowledge gap for CCS site selection. By combining experimental mineralogical and geochemical data with regional geological context, this study advances the understanding of CO_2 - rock interactions in active industrial and petroleum-bearing settings, offering practical insights for optimizing CCS strategies in Thailand and similar sedimentary basins.

Keywords: Carbon capture and storage (CCS), CO_2-rock interaction, Mineral trapping, Khorat Plateau, Geochemistry, Mineralogy, X-ray diffraction (XRD), X-ray fluorescence (XRF)

Introduction

Carbon dioxide (CO_2) emissions from the energy and industrial sectors present a pressing global challenge. In particular, power generation from natural gas and biogas, together with industrial activities such as mining and cement production, constitute major emission sources [1]. In Thailand, a significant proportion of these operations - including 147 licensed mining activities for industrial minerals such as limestone, basalt, sandstone, and rock salt - are concentrated within the Khorat Plateau [1-5]. The geological characteristics of potential storage sites are critical for effectively mitigating CO_2 emissions at their source [1-4].

Four fundamental CO_2 trapping mechanisms in subsurface geological formations, namely

structural/stratigraphic, residual, solubility, and mineral trapping, are shown in **Figure 1** [2], highlighting their roles in ensuring secure and long-term carbon storage. Structural and stratigraphic trapping constitute primary mechanisms, whereby buoyant CO_2 migrates through permeable reservoir rocks until it is halted beneath an impermeable cap rock - such as an anticline, fault-bound structure, or stratigraphic pinch-out - that prevents further upward movement. This form of trapping typically provides the most immediate storage security and is widely applied in CCS projects. Residual trapping occurs when CO_2 becomes immobilized as isolated bubbles within rock pore spaces after the primary CO_2 plume has passed, a process governed by capillary forces that stabilize the gas over short to intermediate timescales. Solubility trapping enhances storage security by dissolving CO_2 into formation water (brine), producing carbonic acid (H_2CO_3), which is denser and more likely to sink, thereby reducing the potential for upward migration; this mechanism operates over intermediate to long timescales. The most permanent form, mineral trapping, involves the reaction of dissolved CO_2 with minerals in the host rock to form stable carbonate phases such as calcite or siderite, resulting in irreversible sequestration over thousands to millions of years. Collectively, these trapping mechanisms underpin the stability and reliability of geological CO_2 storage systems.

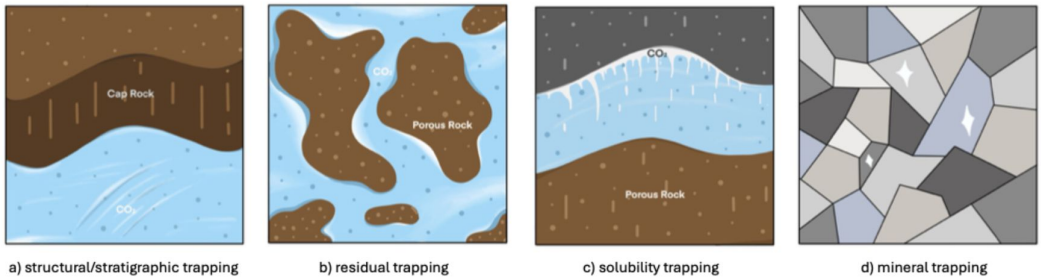

Figure 1 Schematic representation of the 4 principal CO_2 trapping mechanisms in subsurface geological formations relevant to carbon capture and storage (CCS): (a) structural/stratigraphic trapping, (b) residual trapping, (c) solubility trapping, and (d) mineral trapping. Adapted from [2].

The Khorat Plateau is considered a promising region for geological CO_2 storage due to its distinctive geological characteristics [1,3,4]. Previous assessments have identified Permian carbonates as the most favorable storage formations, followed by Khorat Group sandstones and evaporitic rock salt (**Figure 2**), whereas Cenozoic basalts have generally been deemed unsuitable [1]. Chenrai *et al.* [6] further examined gas-bearing shales and the Triassic Huai Hin Lat Formation, showing that its coaly, carbonate-silicate, and carbonate mudstones were deposited in an anoxic to sub-oxic aquatic environment, indicating good storage potential.

Although earlier studies expressed reservations regarding the efficiency of basalt as a long-term CO_2 reservoir - primarily due to uncertainties about reaction kinetics, permeability reduction, and limited field-scale validation - more recent research demonstrates that basalt can effectively facilitate CO_2 sequestration through carbonate mineralization [6-9]. Thermodynamic modeling and high-pressure experiments indicate that basalt reacts readily with CO_2-acidified brines, forming stable carbonate minerals within a temperature range of 50 - 200 °C and pressures around ~300 bar, with maximum reactivity observed near 100 °C [6]. While calcite, magnesite, and siderite are thermodynamically predicted, experimental results identify magnesite as the dominant precipitate (**Figure 3**).

Taksavasu *et al.* [10] also demonstrated the reactivity of ultramafic rocks, particularly olivine-rich wehrlite from Huai Ma Hin, northern Thailand, which showed ~25% alteration to serpentine and chlorite after 5 days at 40 °C and 1 atm. Reactive surface area was a key control on carbonation rates.

Thailand hosts over 30 potential mining sites, including widespread Late Cenozoic basalts in Buriram, Surin, and Sisaket provinces (**Figure 2**) [6,11,12]. Disused mines with existing boreholes offer unique

opportunities for CO_2 injection; however, the chemical reactivity of limestone, basalt, and rock salt under water-saturated CO_2 conditions remains poorly understood [1,6].

This study addresses this gap by evaluating the mineralogical and geochemical reactivity of limestone, basalt, rock salt, and Mesozoic sandstone and calcareous sandstone. Focusing on the Khorat Plateau - characterized by extensive basalt, active mining of Permian limestone, Khorat Group sandstone, and rock salt [5,13,14], and petroleum potential in Permian carbonates sealed by Khorat Group sediments [15] - this work provides new insights into CO_2 injection feasibility in active industrial and petroleum-bearing settings. Laboratory experiments on samples from representative mining and petroleum-related sites (**Figure 2**) are compared with potential field-scale reactions to assess implications for CCS deployment. Unlike previous studies, this research integrates multiple lithologies from both mining and petroleum contexts, providing the 1st comparative reactivity assessment under wet CO_2 conditions for the Khorat Plateau, thereby bridging a critical knowledge gap in regional CCS planning.

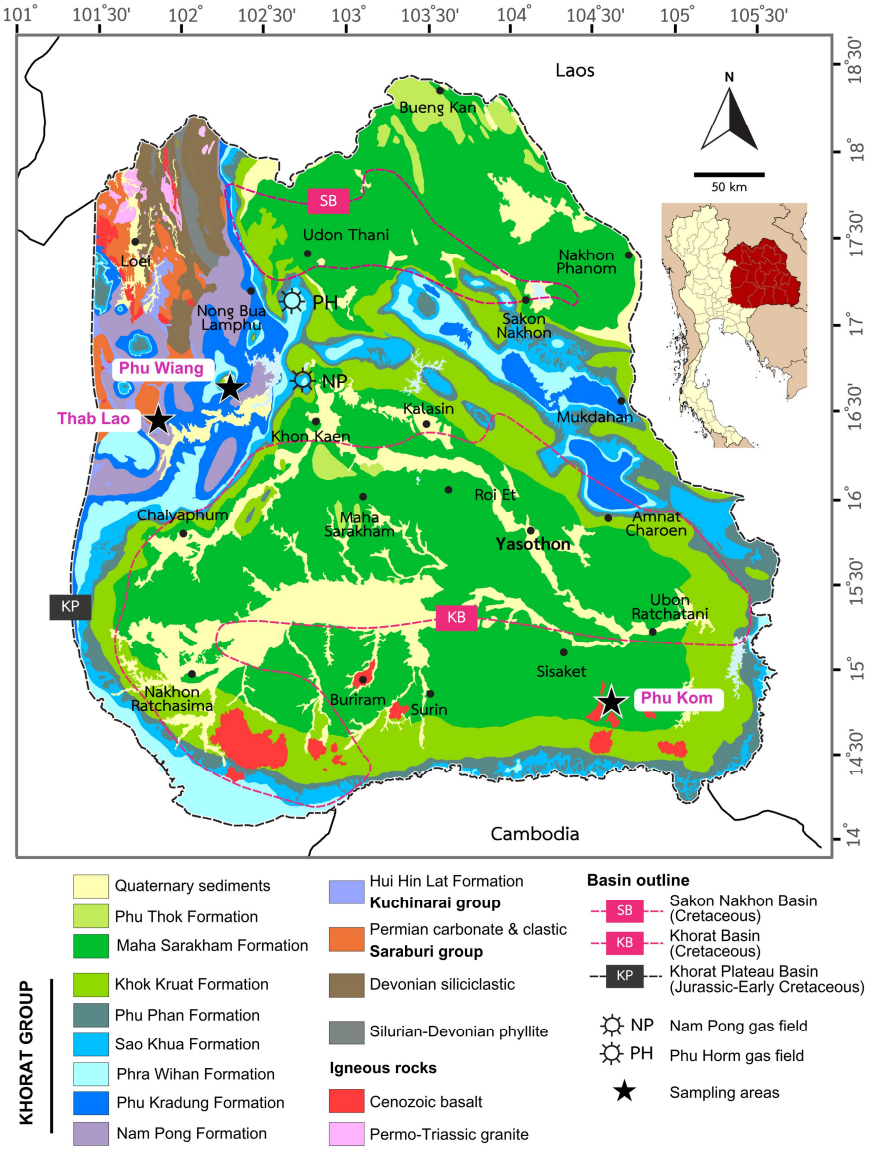

Figure 2 Simplified geological map of the Khorat Plateau showing the main producing gas fields and sampling locations (black stars). Geological data adapted from Geological Survey Division [11].

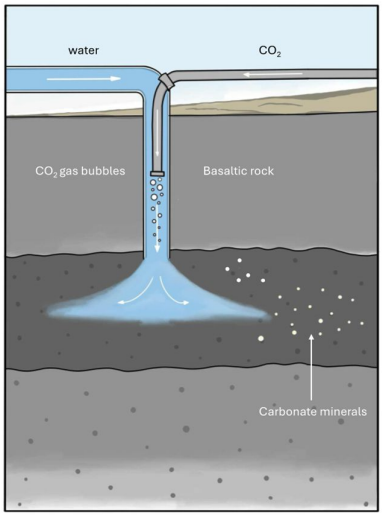

Figure 3 Carbon storage in basaltic rocks, CO_2 is first dissolved in water and then injected into porous basaltic formations. Because the CO_2 is in dissolved form, it is non-buoyant and does not require a cap rock to prevent migration. Solubility trapping occurs immediately upon injection, and within approximately 1 year [8], most of the injected carbon is permanently sequestered through mineralization into stable carbonate minerals.

Materials and methods

This study employed a multi-stage approach to evaluate the chemical reactivity of representative rock types from the Khorat Plateau with CO_2 in the presence of water. Five lithologies were selected - basalt, limestone, sandstone, calcareous sandstone, and rock salt - collected from boreholes and mining sites in Sisaket, Khon Kaen, and Chaiyaphum provinces (**Figure 2**). These locations represent key stratigraphic units: Cenozoic Basalt, the Cretaceous Sao Khua Formation (Ksk), Cretaceous Phra Wihan Formation (Kpw), Cretaceous Maha Sarakham Formation (Kms), and the Permian Pha Nok Khao Formation (Pnk). Sample details, including codes, lithologies, stratigraphic positions, and localities, are summarized in **Table 1**.

Table 1 Sample details and corresponding collection sites, including rock type, stratigraphic formation, and geographic location of each representative specimen analyzed in this study.

Sample	Rock type	Formation	Coordinates (UTM, 48Q)	Collection site
BSG, BSK	basalt	Cenozoic Basalt	433448E 1593190N	Phu Kom, Sisaket Province
SSK	sandstone	Ksk	217378E 1849227N	Wat Chan Khemaram, Khon Kaen Province
SPW	sandstone	Kpw	222418E 1839421N	Phu Wiang National Park, Khon Kaen Province
LSP	limestone	Pnk	805209E 1832831N	Thap Lao Spring Arboretum, Chaiyaphum Province
RS	rocksalt	Kms	216587E 1847412N	Ban Bo, Wiang Kao District, Khon Kaen Province

Thin sections (30 μm thick) were prepared following standard petrographic procedures, including cutting, grinding, polishing, bonding to glass slides with thermoplastic cement, and mounting with Canada balsam. Petrographic observations were performed using a polarized light microscope (Olympus CX31,

Olympus Corporation, Tokyo, Japan) equipped with both transmitted and reflected light capabilities. This allowed for the identification of mineral assemblages, textural relationships, and alteration features prior to CO_2 exposure.

Bulk rock samples were initially crushed using a Retsch BB50 jaw crusher (Retsch GmbH, Haan, Germany) and subsequently pulverized to 200 mesh (~75 μm) using a FRITSCH PULVERISETTE 6 Classic Line Planetary Mono Mill (FRITSCH GmbH, Idar-Oberstein, Germany). The 200-mesh particle size was selected to ensure sufficient surface area for enhancing water-rock interaction and detecting mineralogical changes within practical laboratory timescales. Although this finer grain size may accelerate reaction kinetics compared to natural reservoir conditions, the chosen size allows for a clearer assessment of potential mineral reactivity. Sensitivity analyses for coarser fractions (e.g., 60, 100 and 325 mesh) were not conducted in this study and are recommended for future work to better constrain field-scale extrapolations.

Major element compositions were determined using a handheld X-ray fluorescence (XRF) analyzer (Vanta Series, Olympus Corporation, Tokyo, Japan), with a precision of ± 0.05 wt.% for major oxides. Calibration was performed using USGS-certified rock standards (e.g., BHVO-2, AGV-2), and analytical accuracy was cross-validated with duplicate measurements of randomly selected samples. The resulting elemental concentrations were converted to oxide weight percentages for subsequent geochemical classification and provenance analysis.

Reactivity experiments involved mixing 10 g of powdered sample with 250 mL of distilled water in 600 mL beakers, followed by injection of 3 mL CO_2 gas using a Viza Soda Stream Juice 701 Red system. Beakers were sealed with aluminum foil and stirred magnetically, with reactions conducted at 60 °C and 1 atm for 24 h in a hot-air oven, following conditions optimized by Taksavasu *et al.* [10]. Post-reaction solid residues were filtered, oven-dried at 100 °C, and analyzed using X-ray diffraction (XRD) (Rigaku MiniFlex 600 Benchtop XRD System, Rigaku Corporation, Tokyo, Japan). Samples were mounted as pressed pellets or glass-slide preparations to optimize peak resolution for low-abundance phases. Diffractograms were collected under the following operating conditions: Cu Kα radiation, 40 kV tube voltage, 15 mA tube current, scanning range 5° - 80° 2θ, and step size 0.02°. Data reduction and mineral identification were performed using Rigaku PDXL software (Rigaku Corporation, Tokyo, Japan), with reference to the ICDD PDF-4+ database. Relative phase proportions were semi-quantitatively estimated based on integrated peak intensities.

Results and discussion

Petrographic characteristics of the rock samples

Five representative rock samples were collected from different localities within the Khorat Plateau, northeastern Thailand (Sisaket, Khon Kaen, and Chaiyaphum Provinces; **Figure 2**) for petrographic analysis. The samples represent key lithologies from the region, including Cenozoic basalt (BSG-1), Cretaceous sandstones of the Sao Khua Formation (SSK-2) and Phra Wihan Formation (SPW-2), Cretaceous limestone of the Maha Sarakham Formation (LSP-1), and Permian rock salt of the Pha Nok Khao Formation (RS).

Thin sections were prepared and examined under a polarized light microscope (Olympus CX31) to determine mineral composition, texture, and evidence of alteration. Basalt (BSG-1) - Fine- to medium-grained, porphyritic to intergranular textures with abundant plagioclase and pyroxene phenocrysts set in a microcrystalline to glassy groundmass (**Figure 4(a)**). Olivine is partially altered to serpentine and iddingsite. Secondary minerals include chlorite, talc, and hematite. Sandstone (SSK-2) - Medium-grained litharenite dominated by subangular to subrounded quartz, feldspar, and lithic fragments (**Figure 4(b)**). Clay minerals (kaolinite, illite) occur as pore-filling cement. Iron oxide coatings impart a reddish coloration. Calcareous Sandstone (SPW-2) - Similar framework to SSK-2 but with abundant carbonate cement (calcite and aragonite), locally recrystallized (**Figure 4(c)**). Zeolites (phillipsite, analcime) and clays occur as accessory phases. Limestone (LSP-1) - Sparry calcite and micrite constitute the dominant components of the matrix, accompanied by minor amounts of dolomite and siderite (**Figure 4(d)**). Fossil fragments are locally preserved within the matrix and, based on Folk's classification

scheme [16], the texture can be classified as packed biomicrite. Rock Salt (RS) - Composed entirely of halite with large, interlocking cubic crystals and minor clay inclusions. These petrographic observations highlight the varied lithologies within the Khorat Plateau, providing the basis for evaluating mineralogical and chemical changes following CO_2 interaction.

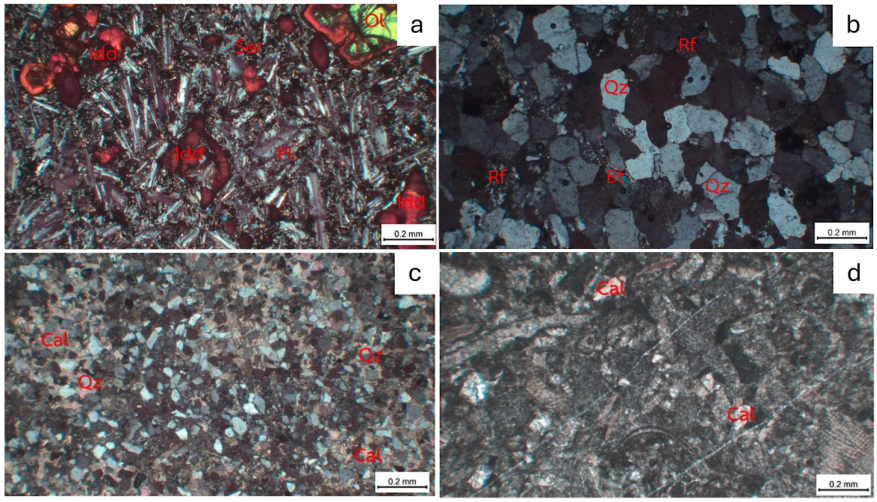

Figure 4 Photomicrographs under cross-polarized light: (a) Olivine basalt (BSG-1) with olivine phenocrysts altered to iddingsite (Idd) in a plagioclase-rich groundmass; (b) Quartz arenite (SSK-2) with quartz (Qz), plagioclase (Pl), biotite (Bt), and rock fragments (Rf); (c) Calcareous sandstone (SPW-2) dominated by quartz (Qz) and calcite (Cal); (d) Packed biomicrite (LSP-1) with micritic matrix and fossil fragments. Abbreviations: Pl - plagioclase, Ol - olivine, Idd - iddingsite, Ser - sericite, Qz - quartz, Bt - biotite, Rf - rock fragments, Cal - calcite.

Whole-rock geochemistry

A total of 11 representative samples were selected across the studied lithologies, including 4 trachybasalts, one alkaline basalt, 3 sandstones, 1 calcareous sandstone, 1 rock salt, and 1 limestone. The sample selection was guided by field mapping, petrographic variability, and accessibility constraints to ensure coverage of the dominant lithological units within the study area. While the limited number of samples in certain lithologies (e.g., basalt, rock salt, limestone) may not fully capture local heterogeneity, these specimens were chosen based on their representativeness of the most characteristic mineralogical and textural features observed in the field.

Whole-rock XRF analysis of untreated samples (**Table 2**) reveals distinct compositional signatures reflecting lithological differences. Basalts are silica-poor ($SiO_2 \approx 45$ wt.%) but enriched in Fe_2O_3, MgO, and CaO, consistent with mafic igneous compositions. Sandstones are quartz-rich with moderate Al_2O_3 and K_2O, whereas calcareous sandstone exhibits elevated CaO due to carbonate cementation. Limestone is dominated by CaO (> 50 wt.%) with minor MgO and low SiO_2, while rock salt is chemically simple, composed almost entirely of Na_2O and Cl.

Table 2 Whole-rock geochemistry of samples before CO_2 reaction.

Sample	Rock name	Major oxides (wt%)								
		MgO	Al_2O_3	SiO_2	P_2O_5	K_2O	CaO	TiO	Fe_2O_3	MnO
BSG-1	Trachy basalt	2.2917	26.2184	36.7132	0.9180	1.5841	5.2597	1.2868	25.5086	0.2196
BSG-2	Trachy basalt	3.2912	24.7103	38.6078	0.7805	3.9672	6.3737	1.3007	20.8664	0.1023
BSG-3	Trachy basalt	2.3294	25.7563	35.8979	0.8919	1.5089	5.2233	1.3513	26.8199	0.2211
BSG-4	Trachy basalt	1.2794	31.6277	33.3135	0.7431	0.8662	2.2037	1.5609	28.2600	0.1455
BSK-1	Basalt (alkaline)	0.0000	32.6332	26.1677	0.4715	0.7877	0.3957	2.4483	36.9660	0.1299

Sample	Rock name	Major oxides (wt%)								
		MgO	Al_2O_3	SiO_2	P_2O_5	K_2O	CaO	TiO	Fe_2O_3	MnO
SPW-1	lith arenite (Slt)	0.0000	20.2314	53.8046	0.0992	2.3474	14.9442	0.6225	7.8313	0.1193
SSK-1	Sub arkose	0.0000	12.0245	85.4635	0.0476	1.1809	0.0614	0.1107	1.0814	0.0301
SPW-2	Calcrete (Subarkose)	0.0000	14.3261	54.8537	0.0967	1.5063	24.9299	0.3571	3.5363	0.3938
SSK-2	Quartz arenite	0.0000	7.0285	91.8221	0.0000	0.5479	0.0613	0.0508	0.4677	0.0216
RS-1	Rocksalt	53.9434	39.8158	2.4988	1.7811	0.0000	1.8048	0.0000	0.1238	0.0324
LSP-1	Packstone	0.0000	0.0000	1.0734	0.0000	0.0000	98.8115	0.0000	0.1151	0.0000

Trace element patterns further differentiate lithologies. Basalt shows enrichment in transition metals (Ni, Cr and V), sandstones have relatively high Zr and Ti from heavy minerals, and limestone contains minor Sr and Ba associated with carbonates. These data provide a baseline for assessing post-reaction geochemical modifications.

Mafic volcanic rocks (BSG-1 to BSG-4, BSK-1) from the Cenozoic volcanic units of Sisaket Province are classified as trachybasalt and alkaline basalt. They contain moderate to high Fe_2O_3 (20.87% - 36.97%), Al_2O_3 (24.71% - 32.63%), and SiO_2 (26.17% - 38.61%), with MgO ranging from 0.00% - 3.29%, reflecting varying magmatic differentiation. BSK-1 has notably evolved, with extreme Fe_2O_3 enrichment (36.97%), no measurable MgO, and low CaO (0.40%), possibly due to alteration or cumulate processes. On the Zr/Ti versus Nb/Y discrimination diagram (**Figure 5(a)**) [17], BSG-1, BSG-2, and BSK-1 plot in the Alkali basalt field, BSG-3 in the Trachyte andesite field, and BSG-4 in the Basanite nepheline field, indicating magmatic diversity from silica-undersaturated to moderately evolved compositions.

Clastic sedimentary rocks (SSK-1, SSK-2, SPW-1, SPW-2) from Khon Kaen Province exhibit high SiO_2 contents, particularly SSK-2 (91.82%) and SSK-1 (85.46%). SPW-2 shows elevated CaO (24.93%), consistent with calcareous cementation. Moderate Al_2O_3 (7.03% - 20.23%) and Fe_2O_3 (0.47% - 7.83%) values indicate mixed detrital input, while low TiO_2 (< 0.7%) and P_2O_5 (< 0.1%) reflect compositional maturity. On the $\log(Fe_2O_3/K_2O)$ versus $\log(SiO_2/Al_2O_3)$ plot (**Figure 5(b)**) [18], SPW-1 plots in the Fe-shale field, SPW-2 in the Wacke field, and SSK-1 and SSK-2 in the Subarkose and Arkose fields, respectively. Non-clastic carbonate rock LSP-1 (PNK Formation, Chaiyaphum Province) is overwhelmingly CaO-rich (98.81%), with minimal SiO_2 (1.07%) and Fe_2O_3 (0.12%), supporting its classification as fossiliferous limestone with a micritic matrix and negligible detrital material. Evaporite rock RS-1 (Khorat Group) consists mainly of MgO (53.94%) and Al_2O_3 (39.82%), with minor SiO_2 (2.50%), CaO (1.80%), and Fe_2O_3 (0.12%). Its chemistry, notably the absence of K_2O and TiO_2, indicates precipitation in a restricted marine or lacustrine evaporitic setting.

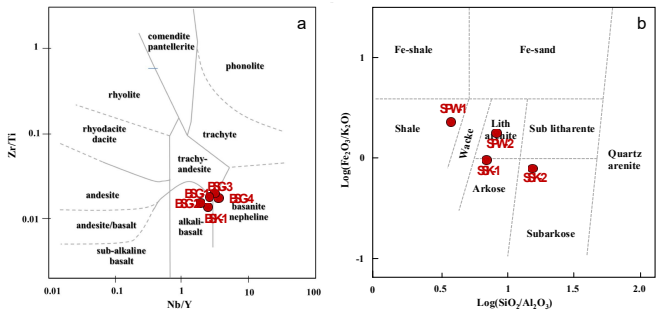

Figure 5 Rock classification based on geochemical characteristics: (a) Classification of volcanic rocks using Zr/Ti versus Nb/Y ratios, modified from Winchester and Floyd [17], showing BSG-1, BSG-2, and BSK-1 in the Alkali basalt field, BSG-3 in the Trachyte andesite field, and BSG-4 in the Basanite nepheline field; (b) Classification of clastic sedimentary rocks using $\log(Fe_2O_3/K_2O)$ versus $\log(SiO_2/Al_2O_3)$ ratios, modified from Herron [18], with SPW-1 plotting in the Fe-shale field, SPW-2 in the Wacke field, and SSK-1 and SSK-2 in the Subarkose and Arkose fields.

Mineralogical changes before and after reaction with CO_2

X-ray diffraction (XRD) analyses reveal distinct mineralogical transformations in all lithologies following CO_2-water interaction, reflecting lithology-dependent dissolution–precipitation reactions and varied capacities for mineral trapping.

Basalt (BSG-1): Prior to reaction, BSG-1 exhibits a diverse igneous mineral assemblage including olivine, plagioclase, pyroxene, hornblende, nepheline, and minor phyllosilicates (serpentine, chlorite, talc), along with accessory hematite, illite, chamosite, and analcite (**Figure 6(a)**). The presence of serpentine and talc suggests pre-existing hydrothermal or weathering alteration. Notably, a broad low-intensity feature (blue circle) indicates an amorphous component, likely alteration products or volcanic glass.

Following CO_2 exposure (**Figure 6(b)**), peak intensities for several reactive phases (olivine, plagioclase, serpentine, illite, chamosite, hornblende) increase (green triangles), suggesting either enhanced crystallinity due to recrystallization or precipitation of secondary minerals with similar structures. Such changes imply that dissolution of labile silicates (e.g., olivine, pyroxene) may release Mg^{2+} and Ca^{2+}, which subsequently reprecipitate as carbonate or hydroxide phases, potentially within microfractures or along grain boundaries. The persistence of the amorphous component suggests incomplete crystallization, possibly representing metastable gels that could evolve into carbonates over longer reaction times. These mineralogical responses indicate that basalt provides both cation sources and reactive surfaces conducive to mineral CO_2 sequestration.

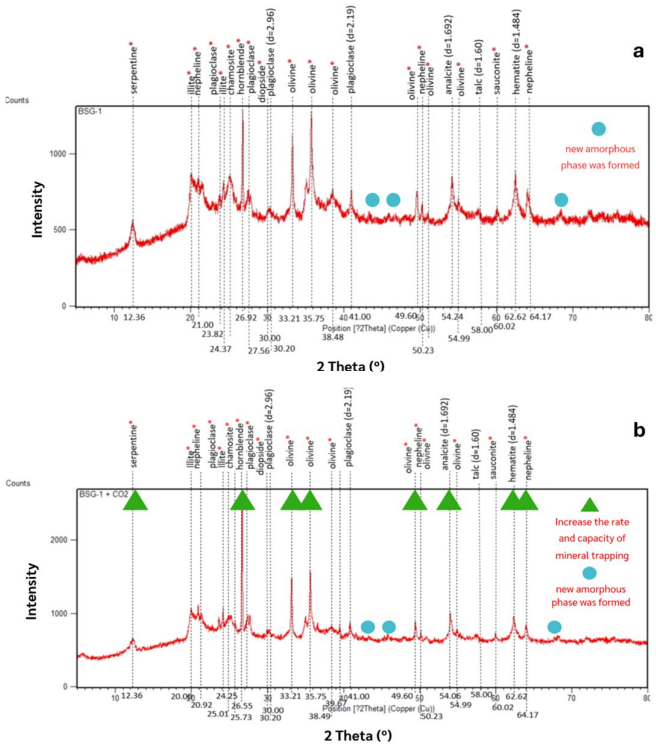

Figure 6 X-ray diffraction (XRD) patterns of basalt sample BSG-1 before (a) and after (b) CO_2-water interaction. (a) The untreated basalt displays a diverse igneous assemblage, including olivine, plagioclase, pyroxene, hornblende, nepheline, serpentine, chlorite, talc, hematite, illite, chamosite, and analcite. The light blue circles highlight a broad, low-intensity region interpreted as an amorphous phase, likely alteration products or volcanic glass. (b) Post-reaction analysis shows increased intensities for several silicate and oxide phases (green triangles), indicating enhanced crystallinity or reprecipitation of secondary minerals. The persistence of the amorphous phase suggests incomplete crystallization, while the intensity changes point to dissolution–precipitation processes enhancing mineral trapping potential in basalt.

Quartz Arenite Sandstone (SSK-2): The untreated sample is dominated by quartz, with subordinate plagioclase, siderite, apatite, kaolinite, gypsum, and gibbsite (**Figure 7(a)**). The high quartz content suggests a mechanically durable but chemically less reactive framework, with limited mineral trapping potential from the silicate fraction.

After reaction (**Figure 7(b)**), the mineralogical assemblage remains largely unchanged, but enhanced peak intensities are observed for gibbsite, kaolinite, and quartz, along with the appearance of goethite. These changes may reflect precipitation from solution of secondary Al-Fe hydroxides, driven by minor dissolution of feldspars or accessory phases. Although the net capacity for carbonate formation in quartz arenite is low, the formation of goethite and enrichment of hydroxide phases could enhance porosity occlusion, influencing reservoir permeability over time.

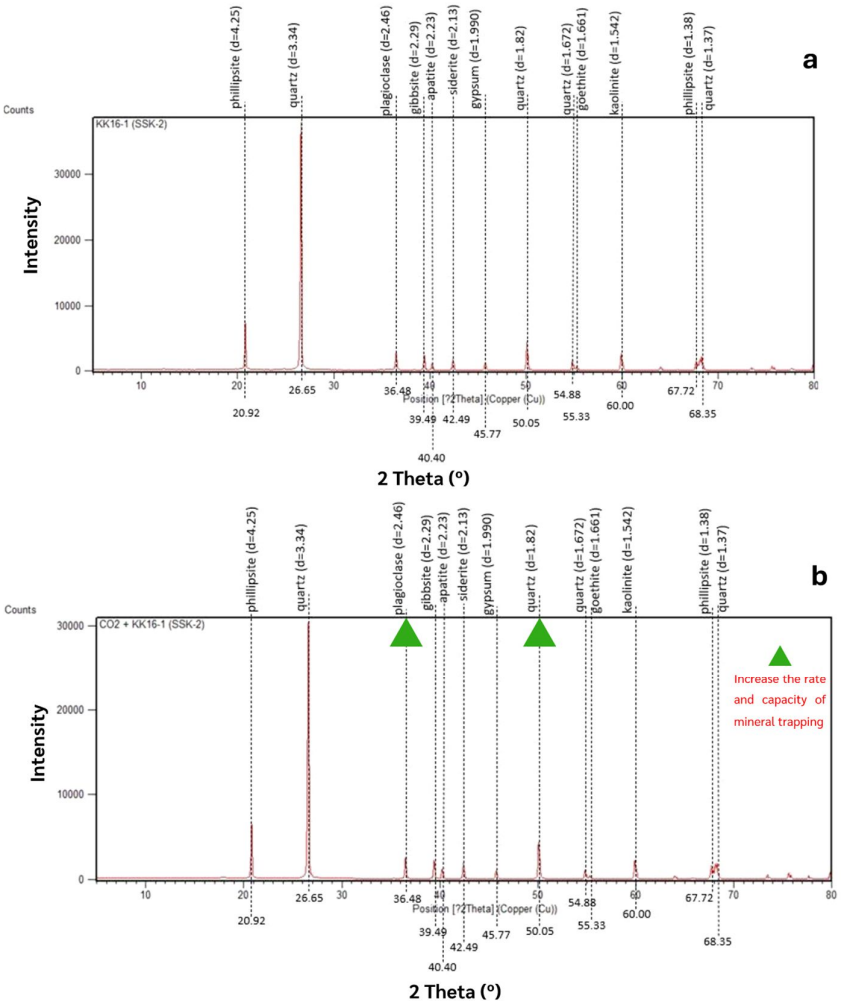

Figure 7 X-ray diffraction (XRD) patterns of quartz arenite sandstone sample SSK-2 before (a) and after (b) CO_2-water interaction. (a) The untreated sandstone is dominated by quartz, with subordinate plagioclase, siderite, apatite, kaolinite, gypsum, and gibbsite. The high quartz peak intensities reflect a mechanically robust but chemically less reactive framework. (b) After reaction, the mineralogy remains largely unchanged, but gibbsite, quartz, and kaolinite peaks increase in intensity (green triangles), and goethite appears. These changes suggest limited silicate dissolution with secondary hydroxide and oxide precipitation, contributing modestly to mineral CO_2 trapping capacity.

Calcareous Sandstone (SPW-2): The pre-reaction assemblage includes calcite, quartz, plagioclase, aragonite, gibbsite, and various zeolites and clays (phillipsite, heulandite, kaolinite, analcime) (**Figure 8(a)**), indicating a mixed carbonate-silicate lithology.

Post-reaction analysis (**Figure 8(b)**) shows minimal change in peak positions or intensities, suggesting that under the experimental conditions, the carbonate fraction did not undergo significant dissolution–precipitation, or that such reactions occurred at rates below the detection limit of bulk XRD. This relative stability could be attributed to carbonate saturation in the experimental fluid, limiting further calcite dissolution. The absence of significant new phases indicates limited mineral trapping reactivity in the short term.

Limestone (LSP-1): Before reaction, LSP-1 is dominated by calcite, with minor aragonite and siderite (**Figure 9(a)**). The sharp, intense calcite peaks indicate high crystallinity and purity of the carbonate phase.

After CO_2-water interaction (**Figure 9(b)**), several new crystalline phases appear, including wollastonite ($CaSiO_3$) and calcium hydroxide ($Ca(OH)_2$), along with a new amorphous component (blue circles). Wollastonite formation suggests dissolution of carbonate phases and reaction with silicate impurities, while $Ca(OH)_2$ precipitation may result from localized oversaturation during calcite dissolution. These transformations indicate a high reactivity of limestone under the tested conditions, with both carbonate dissolution and secondary mineral precipitation potentially contributing to porosity modification and CO_2 immobilization.

Rock Salt (RS): Initially composed entirely of halite (NaCl) (**Figure 10(a)**), the sample is highly crystalline and chemically pure.

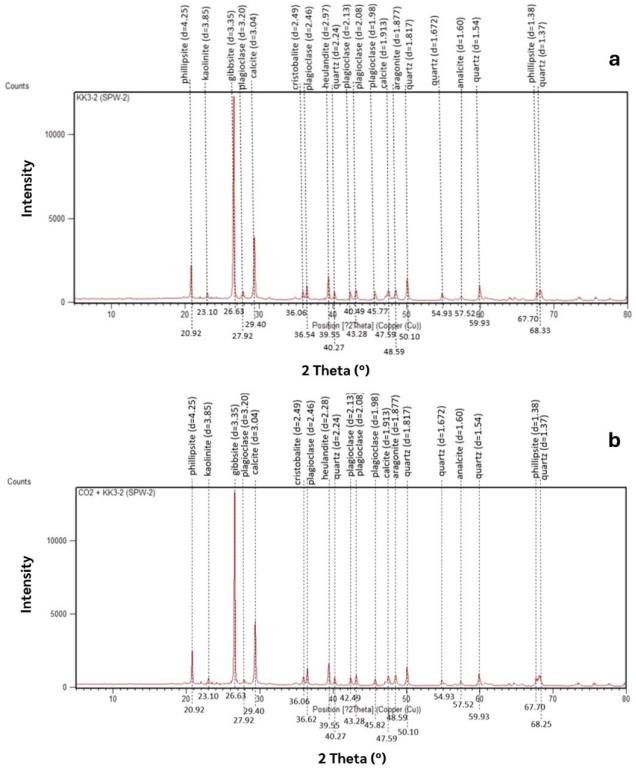

Figure 8 X-ray diffraction (XRD) patterns of calcareous sandstone sample SPW-2 before (a) and after (b) CO_2-water interaction. (a) The untreated sample contains mixed carbonate–silicate phases, including calcite, quartz, plagioclase, aragonite, gibbsite, phillipsite, heulandite, kaolinite, cristobalite, analcime, and ureacronite. (b) After reaction, no significant changes in peak positions or intensities are observed, indicating minimal bulk mineralogical alteration under the experimental conditions. The relative stability may be due to carbonate saturation in solution, limiting dissolution–precipitation reactions in the short term.

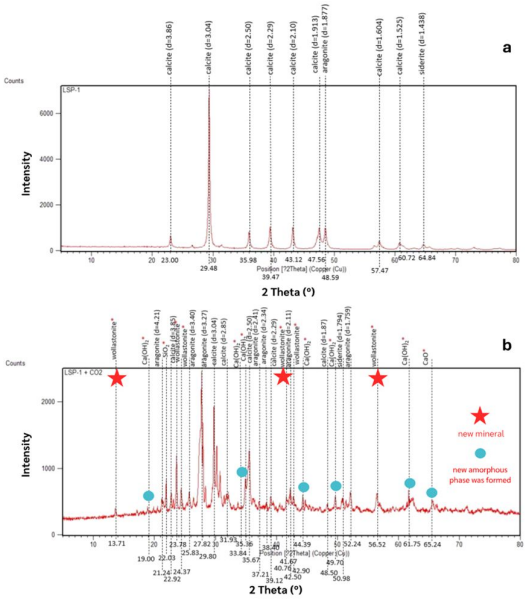

Figure 9 X-ray diffraction (XRD) patterns of limestone sample LSP-1 before (a) and after (b) CO_2-water interaction. (a) The untreated limestone is dominated by calcite, with minor aragonite and siderite, exhibiting sharp, high-intensity peaks characteristic of well-crystallized carbonate phases. (b) Post-reaction, new mineral phases appear, including wollastonite ($CaSiO_3$) and calcium hydroxide ($Ca(OH)_2$) (red stars), alongside a new amorphous phase (light blue circles). These changes indicate dissolution of primary carbonates and subsequent precipitation of silicate and hydroxide minerals, highlighting limestone's high reactivity and strong potential for mineral CO_2 trapping.

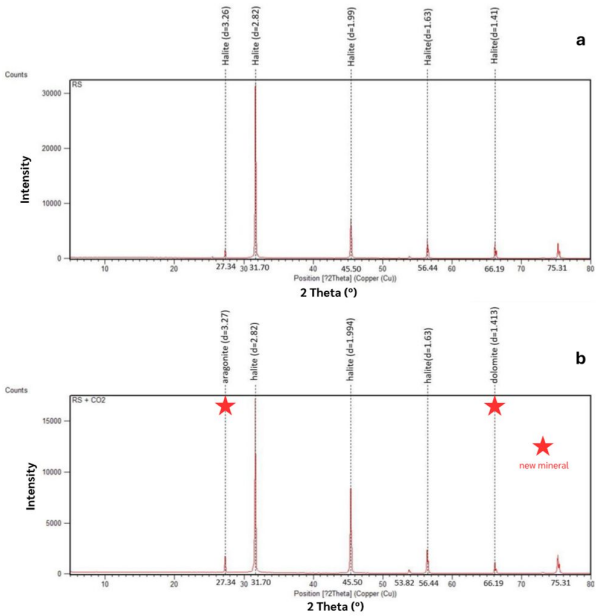

Figure 10 X-ray diffraction (XRD) patterns of rock salt sample RS before (a) and after (b) CO_2-water interaction. (a) The untreated rock salt consists almost entirely of halite (NaCl), with sharp, high-intensity peaks reflecting its purity and crystallinity. (b) After reaction, halite peaks decrease in intensity, and new carbonate phases - aragonite and dolomite - appear, suggesting reaction between CO_2-saturated solution and trace Ca^{2+}/Mg^{2+} impurities in the halite. This demonstrates that even chemically simple evaporites can host localized carbonate precipitation under CO_2 storage conditions.

Post-reaction patterns (**Figure 10(b)**) show reduced halite peak intensities and the emergence of aragonite and dolomite, indicating that even in a predominantly evaporitic lithology, CO_2-water interaction can drive carbonate precipitation, likely from trace Ca^{2+} and Mg^{2+} impurities. This highlights the potential for localized carbonate trapping even in otherwise chemically inert salt formations.

XRD analyses demonstrate pronounced mineralogical changes after CO_2 injection, varying across lithologies according to their primary mineralogy and reactivity (**Figure 11**). Basaltic and limestone samples exhibit the strongest responses, marked by dissolution of Mg-Fe silicates and Ca-carbonates and simultaneous precipitation of new carbonate minerals and gypsum, reflecting efficient CO_2 mineral trapping. In contrast, quartz-rich sandstones show limited reactivity, with only minor secondary hydroxide formation, suggesting a predominantly structural role in CO_2 storage. Notably, rock salt demonstrates carbonate precipitation when impurities are present, expanding its potential as a trapping medium.

These findings highlight that reactive silicate- and carbonate-rich lithologies offer the most promising pathways for long-term mineral carbonation, whereas quartz-dominated sandstones primarily function as passive reservoirs.

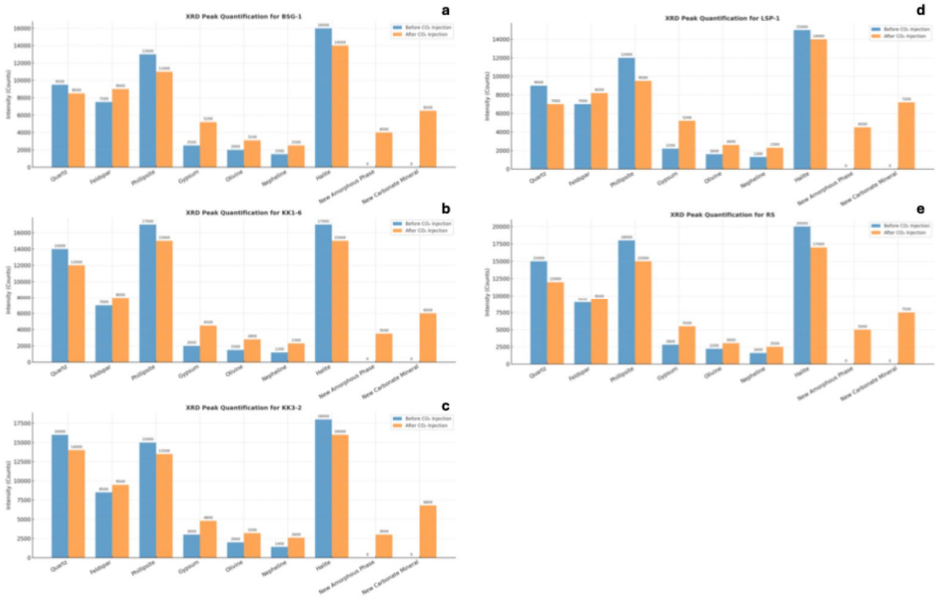

Figure 11 XRD peak quantification of 5 representative samples (BSG-1, KK1-6, KK3-2, LSP-1, RS) before and after CO_2 injection, showing dissolution of primary framework minerals, formation of amorphous phases, and precipitation of secondary carbonates and gypsum, indicating enhanced CO_2 mineral trapping capacity.

CO_2-water-rock interaction experiments

Experimental simulations of CO_2-water-rock interactions under wet conditions revealed distinct lithology-dependent mineralogical and physical changes:

Alkali basalt presented a light brown suspension formed without visible white precipitates. XRD analyses showed alteration of primary mafic minerals into phyllosilicates (chlorite, serpentine, analcime, talc, saponite) and hematite [19], derived from the alteration of olivine, pyroxene, plagioclase, and magnetite as shown in Eq. (1):

Primary silicates + CO_2 + H_2O → Chlorite + Serpentine + Montmorillonite + Talc + Hematite + Carbonic acid (1)

Sandstone produced a light brown suspension with thin white film precipitates, suggestive of kaolinite formation from plagioclase breakdown [20,21] in Eq. (2):

$(Ca,Na,K)_{1-2}Al_{1-2}Si_{2-3}O_8 + CO_2 + H_2O \rightarrow Al_2Si_2O_5(OH)_4 + Al(OH)_3 + H_2CO_3$ (2)

Calcareous sandstone (SPW-2) has no significant mineralogical transformations detected, indicating low reactivity. Meanwhile, limestone exhibited high reactivity with light gray suspensions and thin film precipitates. XRD confirmed new phases-wollastonite ($CaSiO_3$), portlandite ($Ca(OH)_2$), and amorphous CaO-formed via the following reactions in Eqs. (3) - (5).

$$2CaCO_3 + 2SiO_2 + CO_2 + 3H_2O \rightarrow 2CaSiO_3 + 3H_2CO_3 \quad (3)$$

$$2CaCO_3 + CO_2 + 5H_2O \rightarrow 2Ca(OH)_2 + 3H_2CO_3 \quad (4)$$

$$2CaCO_3 + CO_2 + 3H_2O \rightarrow 2CaO + 3H_2CO_3 \quad (5)$$

These results are consistent with previous findings on $CaCO_3$ decomposition and CO_2 capture processes reported by Rodríguez *et al.* [22]. The unexpected wollastonite formation at 100 °C and 1 atm (sample LSP-1) likely reflects kinetic precipitation from highly reactive, finely ground material and CO_2-saturated solutions, rather than thermodynamic stability at low temperatures.

Halite exhibits minimal reactivity with CO_2 under ambient pressure and temperature. Experimental observations revealed a rapid initial temperature increase to 77 °C, resulting from halite dissolution and rapid ion exchange in the electrolyte-rich brine, followed by stabilization at the set point of 60 °C. Post-reaction, white condensates on the aluminum foil indicated halite sublimation and subsequent re-precipitation. No significant new mineral phases formed under the applied conditions (1 atm, 60 °C, 24 h). Nevertheless, theoretical reaction pathways suggest that under elevated temperature and pressure, halite may react with CO_2 and water to produce sodium carbonate and hydrochloric acid [23] (Eq. (6)).

$$2NaCl + CO_2 + H_2O \rightarrow Na_2CO_3 + 2HCl \quad (6)$$

Implications for carbon sequestration in the Khorat Plateau

Basalt exhibits highly effective silicate weathering reactions with CO_2 under wet conditions, leading to the formation of stable carbonate minerals such as magnesite and siderite. These findings are consistent with global basalt sequestration studies and large-scale in situ carbon mineralization experiments [10,16,17,24,25].

Feldspathic sandstones exhibit mild reactivity with CO_2 through secondary clay mineral formation (e.g., kaolinite, smectite), enabling slower but more stable CO_2 trapping mechanisms [9,26,27]. Additionally, petrographic analyses of mafic and ultramafic rocks in northern Thailand highlight their potential for accelerated CO_2 mineralization under enhanced weathering approaches [26]. In contrast, calcareous sandstones demonstrate limited reactivity, likely due to early carbonate buffering effects, suggesting relatively low suitability as a primary CCS host lithology.

In contrast, limestone is highly reactive due to rapid carbonate dissolution; however, this process produces acidic byproducts capable of mobilizing potentially harmful groundwater constituents, thereby raising significant long-term environmental concerns [27-29].

Halite generally exhibits minimal reactivity with CO_2 under ambient pressure and temperature. However, post-reaction XRD patterns reveal reduced halite peak intensities alongside the emergence of aragonite and dolomite, indicating that CO_2-water interactions can induce localized carbonate precipitation, likely sourced from trace Ca^{2+} and Mg^{2+} impurities. In deeper reservoirs, mineral precipitation involving NaCl or sylvite has also been reported, potentially reducing permeability and clogging pore systems or boreholes [30-33]. Despite its overall low capacity for permanent mineral trapping, CO_2 injection into saline aquifers within or adjacent to halite-bearing formations may mitigate sinkhole formation risks through mineral reprecipitation [32,33], although possible adverse impacts on groundwater quality must be considered.

Based on comparative assessments, basalt-rich domains exhibit the highest CO_2 storage potential, estimated at approximately 2.5 - 3.0 Mt CO_2 per km^3, which significantly exceeds that of sandstones (~0.8 - 1.2 Mt CO_2 per km^3) and limestones (< 0.5 Mt CO_2 per km^3), while halite-bearing formations provide only localized trapping capacities. These results emphasize the importance of lithology, reservoir conditions, and fluid chemistry in governing CO_2 mineralization efficiency and storage stability.

Environmental and operational considerations

The experimental simulations were conducted under wet conditions at moderate temperature (~40 °C) and atmospheric pressure, with significant reactivity observed only in fine-grained samples. This implies that effective CO_2 sequestration in the Khorat Plateau may be largely restricted to fractured zones, fault planes, or high-shear domains associated with tectonic deformation or anthropogenic activities such as hydrofracturing and mining [34-37]. While these zones enhance surface reactivity and potential mineral trapping, they also introduce operational risks, including borehole clogging and localized pressure build-up.

In practice, CCS operations typically target deep formations to increase CO_2 pressure and achieve supercritical phase conditions, thereby minimizing undesirable reactions while maximizing storage security [32]. Conversely, shallow CO_2 storage in brine-rich, evaporite-hosted aquifers may induce mineral precipitation that reinforces host rock and reduces collapse risk, albeit with potential impacts on groundwater chemistry and wellbore performance [30-33].

Overall, these results align with recent CCS-focused studies in the Khorat Plateau, underscoring the contrasting reactivity of basalt and limestone. Basalt offers a long-term, low-risk mineral trapping pathway, whereas limestone's high solubility under CO_2-rich conditions elevates the risk of water contamination and compromises structural integrity over time.

Conclusions

Integrated petrographic, geochemical, and mineralogical analyses reveal distinct CO_2-water-rock interaction pathways across representative lithologies of the Khorat Plateau. Basalt exhibits high reactivity under wet conditions, where silicate weathering promotes the formation of stable carbonate phases such as magnesite and siderite, making it the most promising candidate for secure, long-term CO_2 storage. In contrast, limestone shows rapid carbonate dissolution and acidic byproduct formation, increasing the risk of groundwater contamination and structural instability, thus requiring strict environmental safeguards before its use in CCS projects. Feldspathic sandstones display moderate reactivity, enabling gradual yet stable CO_2 immobilization through secondary clay mineral formation, whereas calcareous sandstones show minimal transformation and consequently low sequestration potential. Halite-bearing formations are generally inert under ambient conditions; however, post-reaction XRD results indicate localized carbonate precipitation of aragonite and dolomite from trace Ca^{2+} and Mg^{2+} impurities, suggesting a limited but potential CO_2 trapping capacity. In deeper reservoir scenarios, additional mineral precipitation such as NaCl and sylvite may further reduce porosity and permeability, requiring careful monitoring of injection behavior and groundwater quality. While these findings provide valuable insights into lithology-controlled CCS feasibility, the study is limited by the small number of representative samples and laboratory conditions that may enhance reaction kinetics compared to natural reservoirs. Future research should incorporate expanded sampling, sensitivity analyses under variable grain sizes and CO_2 pressures, and field-scale validation to refine storage capacity estimates under realistic geological settings. Overall, these results underscore the critical influence of lithology, reservoir characteristics, and fluid chemistry on CO_2 sequestration potential. Basalt-rich formations emerge as the most favorable storage targets in northeastern Thailand, whereas carbonate- and evaporite-hosted settings demand comprehensive risk assessments and long-term monitoring. These insights contribute to advancing both regional CCS planning and global strategies for safe, sustainable, and geologically reliable carbon sequestration in tectonically complex sedimentary basins.

Acknowledgements

The author would like to thank the Department of Geotechnology, Faculty of Technology, Khon Kaen University, Thailand for providing laboratory facilities, experimental equipment, and analytical instruments, including the geochemical laboratory, thin section preparation room, portable X-ray fluorescence (p-XRF), X-ray diffraction (XRD), and polarized light microscope.

Declaration of generative AI in scientific writing

During the preparation of this work, the authors used ChatGPT-5.0 to improve clarity and language quality. All scientific content, interpretations, and conclusions were developed independently by the

authors. After using this tool/service, the authors reviewed and edited the content as needed and take full responsibility for the final version of the publication.

CRediT author statement

Vimoltip Singtuen: Conceptualization, Methodology, Software, Validation, Formal Analysis, Investigation, Resources, Data Curation, Writing – Original Draft, Writing – Review & Editing, Visualization, Supervision, Project Administration. **Juthatip Khonman**: Conceptualization, Methodology, Software, Validation, Formal Analysis, Investigation, Resources, Data Curation, Writing – Original Draft. **Puracheth Rithchumpon**: Methodology, Resources, Writing – Original Draft, Writing – Review & Editing. All authors have read and agreed to the published version of the manuscript.

References

[1] P Chenrai, S Jitmahantakul, R Bissen and T Assawincharoenkij. A preliminary assessment of geological CO_2 storage in the Khorat Plateau, Thailand. *Frontiers in Energy Research* 2022; **10**, 909898.

[2] A Sori and J Moghaddas. A synergistic approach to CO_2 sequestration: Evaluating trapping mechanisms in saline aquifers. *Chemical Product and Process Modeling* 2025; **20(3)**, 419-443.

[3] V Thanasaksukthawee, T Patthanaporn, N Bangpa, A Suwannathong, N Tippayawong, H Shin and S Tangparitkul. Assessing the geological storage capacity of CO_2 in Khorat Sandstone: Geochemistry and fluid flow examinations. *International Journal of Greenhouse Gas Control* 2025; **141(1)**, 104322.

[4] N Suwannakarn and PA Salam. Assessment of land-based negative emissions options in Thailand. *Carbon Management* 2024; **15(1)**, 2372318.

[5] Department of Primary Industries and Mines (DPIM). Data on the number of operating mining concessions in Northeastern Thailand (*in Thai*), Available at: https://www1.dpim.go.th, accessed December 2024.

[6] P Chenrai, T Assawincharoenkij, S Jitmahantakul and P Chaiseanwang. Geochemical characteristics of shale gas formation and the potential for carbon storage in Thailand: An example from the Triassic Huai Hin Lat formation. *Frontiers in Earth Science* 2022; **10**, 1085869.

[7] RJ Rosenbauer, B Thomas, JL Bischoff and J Palandri. Carbon sequestration via reaction with basaltic rocks: Geochemical modeling and experimental results. *Geochimica et Cosmochimica Acta* 2012; **89**, 116-133.

[8] SR Gislason and EH Oelkers. Carbon storage in basalt. *Science* 2014; **344(6182)**, 373-374.

[9] S O Snaebjörnsdottir, F Wisse, T Fridriksson, H Ármansson, GM Einarsson and SR Gislason. CO_2 storage potential of basaltic rocks in Iceland and the oceanic ridges. *Energy Procedia* 2014; **63(29)**, 4585-4600.

[10] T Taksavasu, P Arin, T Khatecha and S Kojinok. Microtextural characteristics of ultramafic rock-forming minerals and their effects on carbon sequestration. *Minerals* 2024; **14(6)**, 597.

[11] Geological Survey Division. Geological map of Thailand in scale of 1:1,000,000, Available at: https://arcg.is/0Wiv0S, accessed December 2024.

[12] V Singtuen and A Anumart. Characterisation and evaluation of columnar basalt geoheritage in Thailand: Implication for geotourism management in post-quarrying area. *Quaestiones Geographicae* 2022; **41(1)**, 37-50.

[13] A Hoffmann and S Siegesmund. The dimension stone potential of Thailand - overview and granite site investigations. *Geological Society London Special Publications* 2007; **271(1)**, 43-54.

[14] LJ Shen and N Siritongkham. The characteristics, formation and exploration progress of the potash deposits on the Khorat Plateau, Thailand and Laos, Southeast Asia. *China Geology* 2020; **3(1)**, 67-82.

[15] S Jitmahantakul, P Chenrai, T Chaianansutcharit, T Assawincharoenkij, A Tang-on and P Pornkulprasit. Dynamic estimates of pressure and CO_2-storage capacity in carbonate reservoirs in a depleted gas field, northeastern Thailand. *Case Studies in Chemical and Environmental Engineering* 2023; **8(9)**, 100422.

[16] RL Folk. Practical petrographic classification of limestones. *AAPG Bulletin* 1959; **43(1)**, 1-38.

[17] JA Winchester and PA Floyd. Geochemical discrimination of different magma series and their differentiation products using immobile elements. *Chemical Geology* 1977; **20**, 325-343.

[18] M M Herron. Geochemical classification of terrigenous sands and shales from core or log data *Journal of Sedimentary Research* 1988; **58(5)**, 820-829.

[19] V Singtuen, S Phajan, A Anumart, B Phajuy, K Srijanta and S Promkotra. Alteration of high alkaline and alkaline basaltic rocks: Parent rocks in the Lava Durian orchard, Sisaket Province, NE Thailand. *Heliyon* 2022; **7(12)**, E08619.

[20] V Singtuen and B Phajuy. Geochemistry and alteration of Lampang - Tak Volcanic Rocks, Thailand. *Suranaree Journal of Science and Technology* 2022; **29(5)**, 030081-8).

[21] FJ Huertas, S Fiore, F Huertas and J Linares. Experimental study of the hydrothermal formation of kaolinite. *Chemical Geology* 1999; **156(1-4)**, 171-190.

[22] N Rodríguez, M Alonso, G Grasa and JC Abanades. Process for capturing CO_2 arising from the calcination of the $CaCO_3$ used in cement manufacture. *Environmental Science & Technology* 2008; **42(18)**, 6980-6984.

[23] F Amrouche, M Bessaïh and M Mounir. Geochemical reactivity of halite with CO_2-rich fluids under simulated subsurface conditions. *Geosciences* 2023; **13(6)**, 161.

[24] JM Matter, M Stute, SÓ Snaebjörnsdóttir, EH Oelkers, SR Gislason, ES Aradottir, B Sigfusson, I Gunnarsson, H Sigurdardottir and E Gunnlaugsson. Rapid carbon mineralization for permanent disposal of anthropogenic carbon dioxide emissions. *Science* 2016; **352(6291)**, 1312-1314.

[25] BP McGrail, HT Schaef, AM Ho, YJ Chien, JJ Dooley and CL Davidson. Potential for carbon dioxide sequestration in flood basalts. *Journal of Geophysical Research* 2006; **111(B12)**, 1-13.

[26] T Taksavasu. Petrographic analysis of mafic and ultramafic rocks in northern Thailand: Implications for CO_2 mineralization and enhanced rock weathering approach. *Geosciences* 2025; **15(3)**, 89.

[27] J Hartmann, AJ West, P Renforth, P Köhler, CLL Rocha, DA Wolf-Gladrow, HH Dürr and J Scheffran. Enhanced chemical weathering as a geoengineering strategy to reduce atmospheric carbon dioxide, supply nutrients, and mitigate ocean acidification. *Reviews of Geophysics* 2013; **51(2)**, 113-149.

[28] A Klemme, T Rixen, M Müller, J Notholt and T Warneke. Destabilization of carbon in tropical peatlands by enhanced weathering. *Communications Earth & Environment* 2022; **3**, 212.

[29] V Vandeginste, C Lim and Y Ji. Exploratory review on environmental aspects of enhanced weathering as a carbon dioxide removal method. *Minerals* 2024; **14(1)**, 75.

[30] L Ji. Coupled flow simulation and geomechanical modeling on CO_2 storage in a saline aquifer. *Earth Sciences* 2018; **7(5)**, 216-226.

[31] OM Ogundipe and EJ Mackay. Modelling halite precipitation during CO_2 injection in a heterogeneous reservoir: A North Sea field case. *In:* Proceedings of the SPE International Conference on Oilfield Chemistry, Galveston, Texas, USA. 2025, p. 15-16.

[32] N Smith, P Boone, A Oguntimehin, G van Essen, R Guo, MA Reynolds, L Friesen, MC Cano and S O'Brien. Quest CCS facility: Halite damage and injectivity remediation in CO_2 injection wells. *International Journal of Greenhouse Gas Control* 2022; **119**, 103718.

[33] M Jin, A Ribeiro, E Mackay, L Guimarães and U Bagudu. Geochemical modelling of formation damage risk during CO_2 injection in saline aquifers. *Journal of Natural Gas Science and Engineering* 2016; **35(A)**, 703-719.

[34] W Xiong, RK Wells, AH Menefee, P Skemer, BR Ellis and DE Giammar. CO_2 mineral trapping in fractured basalt. *International Journal of Greenhouse Gas Control* 2017; **66**, 204-217.

[35] D Liu, R Agarwal, Y Li and S Yang. Reactive transport modeling of mineral carbonation in unaltered and altered basalts during CO_2 sequestration. *International Journal of Greenhouse Gas Control* 2019; **85(9)**, 109-120.

[36] Y Song, S Jun, Y Na, K Kim, Y Jang and J Wang. Geomechanical challenges during geological CO_2 storage: A review. *Chemical Engineering Journal* 2023; **456**, 140968.

[37] IPCC. Carbon dioxide capture and storage, Available at: https://www.ipcc.ch/report/carbon-dioxide-capture-and-storage, accessed June 2025.